Angular momentum properties of hybrid cylindrical vector vortex beams in tightly focused optical systems

Meng, Peiwen; Man, Zhongsheng; Konijnenberg, A. P.; Urbach, H. P.

DOI
10.1364/OE.27.035336

Publication date
2019

Document Version
Final published version

Published in
Optics Express

Citation (APA)
Meng, P., Man, Z., Konijnenberg, A. P., & Urbach, H. P. (2019). Angular momentum properties of hybrid cylindrical vector vortex beams in tightly focused optical systems. *Optics Express*, *27*(24), 35336-35348. https://doi.org/10.1364/OE.27.035336

Important note
To cite this publication, please use the final published version (if applicable).
Please check the document version above.

Research Article | Vol. 27, No. 24 / 25 November 2019 / Optics Express 35336
Optics EXPRESS

Angular momentum properties of hybrid cylindrical vector vortex beams in tightly focused optical systems

PEIWEN MENG,[1,6] ZHONGSHENG MAN,[1,2,4,5] A. P. KONIJNENBERG,[1,3] AND H. P. URBACH[1]

[1]Optics Research Group, Department of Imaging Physics, Delft University of Technology, Lorentzweg 1, 2628 CJ Delft, The Netherlands
[2]School of Physics and Optoelectronic Engineering, Shandong University of Technology, Zibo 255049, China
[3]ASML Netherlands B.V., Veldhoven, The Netherlands
[4]Collaborative Innovation Center of Light Manipulations and Application, Shandong Normal University, Jinan 250358, China
[5]zsman@sdut.edu.cn
[6]p.meng@tudelft.nl

Abstract: Optical angular momenta (AM) have attracted tremendous research interest in recent years. In this paper we theoretically investigate the electromagnetic field and angular momentum properties of tightly focused arbitrary cylindrical vortex vector (CVV) input beams. An absorptive particle is placed in focused CVV fields to analyze the optical torques. The spin-orbit motions of the particle can be predicted and controlled when the influences of different parameters, such as the topological charge, the polarization and the initial phases, are taken into account. These findings will be helpful in optical beam shaping, optical spin-orbit interaction and practical optical manipulation.

1. Introduction

Optical beams have been known to carry angular momentum (AM) [1–3], which expresses the amount of dynamical rotation in the electromagnetic field. There are two distinct forms of AM: spin angular momentum (SAM) and orbital angular momentum (OAM) [4–7]. The former is related to the optical polarization and in particular to circular polarization. The latter depends on the fundamental characteristics of electromagnetic fields, and in particular on the wavefront shape. The SAM can make the particle spin around its own axis [8,9], while the OAM can make the particle orbit around the optical axis [10,11]. Generally, the two different AM forms are independent, but they can interact and be mutually coupled in specific optical processes such as in inhomogeneous or anisotropic media [12–14] and tightly focusing of circularly polarized beams [15].

In recent years, transverse optical SAM, which is perpendicular to the direction of propagation, has attracted intensive attention for its practical applications in microscopy, particle trapping [16,17] and manipulation, especially in high numerical aperture (NA) focusing system [18–21]. When tightly focusing light, one needs to take into account the polarization state of the light. Cylindrical vector vortex (CVV) optical fields have raised a great deal of interest due to their unique polarization and focusing properties [22–24]. Two extreme cases are radially polarized vortex (RPV) and azimuthally polarized vortex (APV) beams. Previous research work that was mainly on OAM can induce localized SAM in the strong focusing of spin-free linearly, radially, azimuthally, and cylindrically polarized beams [19–21,25,26]. However, when a CVV beam is focused, other optical properties including initial phase, topological charge and optical torque should be considered and exploited.

#376417 https://doi.org/10.1364/OE.27.035336
Journal © 2019 Received 27 Aug 2019; revised 26 Sep 2019; accepted 12 Oct 2019; published 18 Nov 2019

Optics EXPRESS

In this paper, we study the spinning dynamics of particles with highly focused CVV input beams. With the Richards and Wolf formulas for the calculation of focused field of an arbitrary CVV beam, we can theoretically obtain all components of the electromagnetic field near focus in a high NA optical system, as well as SAM densities of the focused field. The interaction and transfer between spin- and orbital AM are also shown and discussed. Furthermore, the absorptive trapped particle is introduced to discuss the influences of optical torque on the motions of the particle. We consider optical field with different parameters like topological charge, polarization state and initial phase angles, which may have potential in optical manipulation processes, practical optical trapping, laser structuring of materials [27–29] and optical communications [30,31].

2. Local SAM of focal field for CVV beams

A generalized CVV beam can be written as a linear superposition of a cylindrically symmetric RPV beam and a cylindrically symmetric APV beam, which are given by [32]

$$\begin{aligned}\mathbf{E}_0 &= A_0 e^{im\varphi}(\cos\varphi_0\hat{\mathbf{e}}_r + \sin\varphi_0\hat{\mathbf{e}}_\varphi)\\ &= A_0 e^{im\varphi}[\cos(\varphi+\varphi_0)\hat{\mathbf{e}}_x + \sin(\varphi+\varphi_0)\hat{\mathbf{e}}_y],\end{aligned} \tag{1}$$

where A_0 is a constant determining the relative amplitude distributions of the input optical field, φ and φ_0 represent the azimuthal angle and initial phase, respectively. $\hat{\mathbf{e}}_r$ and $\hat{\mathbf{e}}_\varphi$ are the unit vectors along the radial and azimuthal directions in the polar coordinate system. m denotes the topological charge of the CVV beam. An optical vortex beam with the azimuthal vortex phase $\exp(im\varphi)$ can be physically interpreted as light that has OAM of $m\hbar$ per photon. For $m = 0$, the polarization distributions of CVV beams with different initial phases $\varphi_0 = 0,\ \pi/6,\ \pi/4,\ \pi/3,\ \pi/2$ are shown in Fig. 1. In particular, $\varphi_0 = 0$ and $\pi/2$, correspond to two special CVV beams: RPV and APV beams.

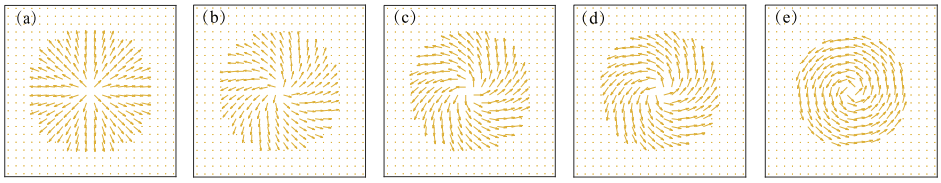

Fig. 1. Polarization distributions of CVV beams with φ_0 = (a) 0, (b) $\pi/6$, (c) $\pi/4$, (d) $\pi/3$, and (e) $\pi/2$, respectively, when the topological charge $m = 0$.

For tightly focusing optical systems, vectorial theory is needed to accurately describe the field near the focal plane. Originating from Ignatovsky's diffraction theory [33], later studied in detail in [34,35], the solution is referred to the vectorial Richard-Wolf integrals. When focused in a homogeneous medium with a real-valued refractive index n, the electric and magnetic fields in the focal region can be expressed as [36]

$$\begin{aligned}\mathbf{E}(r,\ \phi,\ z) &= \frac{-ikf}{2\pi}\int_0^{2\pi}\int_0^{\theta_{\max}}\sqrt{\cos\theta}\,l(\theta)\sin\theta e^{im\varphi}\mathbf{M}_e\exp(i\mathbf{k}\cdot\mathbf{r})d\theta d\varphi,\\ \mathbf{H}(r,\ \phi,\ z) &= \frac{-ikf}{2\pi}\int_0^{2\pi}\int_0^{\theta_{\max}}\sqrt{\cos\theta}\,l(\theta)\sin\theta e^{im\varphi}\mathbf{k}\times\mathbf{M}_e\exp(i\mathbf{k}\cdot\mathbf{r})d\theta d\varphi,\end{aligned} \tag{2}$$

where the wave numbers are $k = k_0 n$ in the medium and $k_0 = 2\pi/\lambda_0$ in free space, with λ_0 the wavelength in vacuum; f is the focal distance, and the maximum tangential angle $\theta_{\max}$ =

Optics EXPRESS

arcsin(NA/n) is determined by the objective lens; θ and φ represent, respectively, the tangential angle with respect to z axis and the azimuthal angle with respect to x axis. $\mathbf{M}_e$ is the propagating unit electric polarization vector in the image plane. $\mathbf{k} = (-\sin\theta\cos\varphi, -\sin\theta\sin\varphi, \cos\theta)$ is the unit vector of the wave vector; $\mathbf{r} = (r_s\cos\phi_s,\ r_s\sin\phi_s,\ z_s)$ is the position vector of an arbitrary point in the image space, and r_s and ϕ_s denote the polar coordinates in a plane z_s. $l(\theta)$ is the entrance pupil amplitude, which is related to Bessel-Gaussian beam [36], here

$$l(\theta) = \exp\left[-\beta^2\left(\frac{\sin\theta}{\sin\theta_{\max}}\right)^2\right]J_1\left(2\beta\frac{\sin\theta}{\sin\theta_{\max}}\right), \tag{3}$$

where β is the ratio of pupil radius to the beam waist and J_1 is the first-order Bessel function of the first kind. In this paper, simulations are performed with the parameters NA= 0.9, $\lambda_0 = 633nm$, and $\beta = 1.0$. The electric polarization vectors $\mathbf{M}_e$ in Eq. (2), can be shown to be

$$\mathbf{M}_e = \begin{bmatrix} -\sin\varphi_0\sin\varphi + \cos\varphi_0\cos\theta\cos\varphi \\ \sin\varphi_0\cos\varphi + \cos\varphi_0\cos\theta\sin\varphi \\ -\cos\varphi_0\sin\theta \end{bmatrix}, \tag{4}$$

thus,

$$\mathbf{k}\times\mathbf{M}_e = \begin{bmatrix} -\cos\varphi_0\sin\varphi - \sin\varphi_0\cos\theta\cos\varphi \\ \cos\varphi_0\cos\varphi - \sin\varphi_0\cos\theta\sin\varphi \\ -\sin\varphi_0\sin\theta \end{bmatrix}, \tag{5}$$

Integrating along the azimuthal direction in Eq. (2), we can obtain the electric fields of an arbitrary CVV beam in the focal region in cylindrical coordinates $(r_s,\ \phi_s,\ z_s)$

$$\mathbf{E}(r,\ \phi,\ z) = \frac{-ikf}{2}\int_0^{\theta_{\max}} l(\theta)\mathbf{P}_m\sqrt{\cos\theta}\sin\theta\exp\left(ikz_s\sin\theta\right)d\theta, \tag{6}$$

where the polarization vector $\mathbf{P}_m$ is

$$\mathbf{P}_m = i^m e^{im\phi_s}\begin{bmatrix} i[J_{m+1}(\xi) - J_{m-1}(\xi)]\cos\varphi_0\cos\theta - [J_{m+1}(\xi) + J_{m-1}(\xi)]\sin\varphi_0 \\ [J_{m+1}(\xi) + J_{m-1}(\xi)]\cos\varphi_0\cos\theta - i[J_{m+1}(\xi) - J_{m-1}(\xi)]\sin\varphi_0 \\ 2J_m(\xi)\cos\varphi_0 \end{bmatrix}. \tag{7}$$

Here $\xi = kr_s\sin\theta$ and $J_m(\xi)$ is the mth-order Bessel function of the first kind.

For an arbitrary time-harmonic beam, the time-averaged SAM density can be written as [6,37]

$$\mathbf{S} = \frac{\mathrm{Im}[\epsilon(\mathbf{E}^*\times\mathbf{E}) + \mu(\mathbf{H}^*\times\mathbf{H})]}{4\omega}, \tag{8}$$

where ω is the angular frequency of the light beam. The superscript $*$ denotes the complex conjugate and Im[z] denotes the imaginary part of z. Compared with the dominant interaction between the electric field and particles in nature, the magnetic field acts weakly on them. Therefore, we only take the SAM originated from the electric field into account. Then the three

Optics EXPRESS

orthogonal components of **S** are in cylindrical coordinates given by

$$\begin{aligned} S_r &= \frac{\epsilon}{4\omega}\mathrm{Im}(E_\phi^* E_z - E_\phi E_z^*), \\ S_\phi &= \frac{\epsilon}{4\omega}\mathrm{Im}(E_z^* E_r - E_z E_r^*), \\ S_z &= \frac{\epsilon}{4\omega}\mathrm{Im}(E_r^* E_\phi - E_r E_\phi^*). \end{aligned} \tag{9}$$

Now we first investigate the focusing properties of the CVV beams in free space. The intensity distributions of the electric fields in the focal plane of CVV beams with $\varphi_0 = 0, \pi/4, \pi/3, \pi/2$ and $-\pi/4$, when the topological charge $m = 0$ are shown in Fig. 2. For the illumination without OAM ($m = 0$), it is well known that the radial component is a donut shape and the azimuthal component is zero while the longitudinal component is strongly centered when $\varphi_0 = 0$, which corresponds to an RPV beam in Figs. 2(a_1)–2(d_1) . When increasing of φ_0, the intensities of both radial and longitudinal components decrease while the intensities of the azimuthal components increase. In the extreme case $\varphi_0 = \pi/2$ only azimuthal component exists, which corresponds to the APV beam shown in Figs. 2(a_4)–2(d_4). It can be seen in Figs. 2(a_2)–2(d_2) and Figs. 2(a_5)–2(d_5) that the intensities do not change, when the initial phase φ_0 changes from $\pi/4$ to $-\pi/4$. Figure 3 shows the normalized SAM density distributions of the corresponding focused CVV input beams in Fig. 2. All the SAM density profiles are donut-shaped and the longitudinal SAM densities S_z remain zero, because such focal field has a purely transverse SAM locally [38]. From Eq. (9), when there is no OAM ($m = 0$), it can be easily found that the radial and longitudinal SAM densities equal zero with the RPV illumination shown in Fig. 3(a_1)–3(c_1) because of the lack of an azimuthal component. Similarly and also interestingly, with the APV illumination, there are no SAM densities at all as in Figs. 3(a_4)–3(c_4). Apart from these two extreme conditions, for other initial phases, the focal fields all carry transverse SAM densities S_r and S_ϕ. Moreover, the signs between the radial and azimuthal SAM densities are opposite whenever the initial phase φ_0 is positive. It is worth noting that when $\varphi_0 = -\pi/4$, as seen in Figs. 3(a_5) and 3(b_5), the sign of S_r changes to positive while S_ϕ keeps the same sign compared with Figs. 3(a_2) and 3(b_2).

Next, we discuss the influence of the topological charge m on the local spin state. For comparison, we start again from the focal field profiles of CVV beams with $m = 1$ and $\varphi_0 = 0$, $\pi/4$, $\pi/3$, $\pi/2$ and $-\pi/4$ in Fig. 4. As opposed to focusing CVV beams without OAM in Fig. 2, the CVV beams with $m = 1$ generate solid focal spots. The donut-shaped longitudinal intensities disappear gradually with the increase of the initial phase φ_0, while the focal spots get increasingly sharper as seen in Figs. 4(d_1)–4(d_4). The special cases of field distributions generated by RPV and APV beams are shown in Figs. 4(a_1)–4(d_1) and Figs. 4(a_4)–4(d_4), respectively. It is well known and widely used that the RP beam provides tight focus, but the focal spot of APV beam with $m = 1$ shown in Fig. 4(d_4) gives the smallest size compared with focal spots given by RPV beams as shown in Fig. 2(d_1). This fact was noted in earlier work [39] and can be used for improving the resolution of optical imaging systems. Figure 5 gives the results of SAM density distributions of the corresponding focused CVV input beams with $m = 1$ as in Fig. 4. In Fig. 5 one observes similar as in Fig. 3, but in addition one can notice that the purely transverse spin states in Fig. 3 change to three components here. Strong longitudinal SAM densities appear in the focal plane and dominate in three components, even in the special cases of RPV and APV input beams. The SAM densities of the other two components are getting weaker, which means the properties of the local spin state have been converted. Obviously, the varying ratios between transverse and longitudinal SAM densities is because of different initial phases and the induced OAM. To avoid the misunderstanding, we should point out that the global axial SAM S_z is zero, which can be validated by numerically integrating the S_z density over the whole focal plane.

To explore further the influences of the initial phases and OAM on the distributions of SAM density, Fig. 6 depicts the normalized cross sections of SAM densities in the focal plane of

Optics EXPRESS

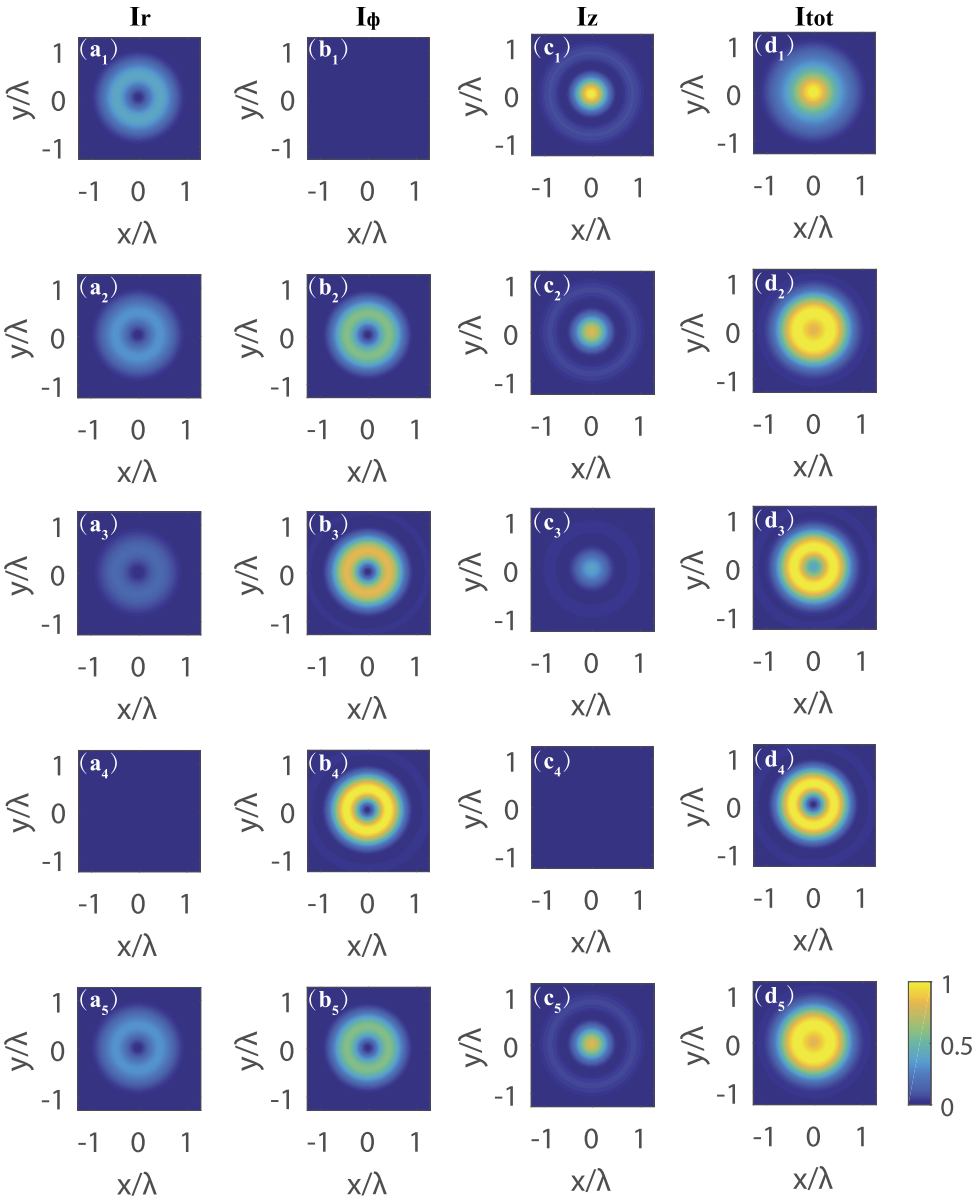

Fig. 2. Electric field intensity distributions in the focal plane of CVV beams with $\varphi_0 = 0$, $\pi/4$, $\pi/3$, $\pi/2$ and $-\pi/4$ (rows 1-5, respectively), when the topological charge $m = 0$. All the intensities are normalized to the maximum intensities near focus for each illumination mode.

Optics EXPRESS

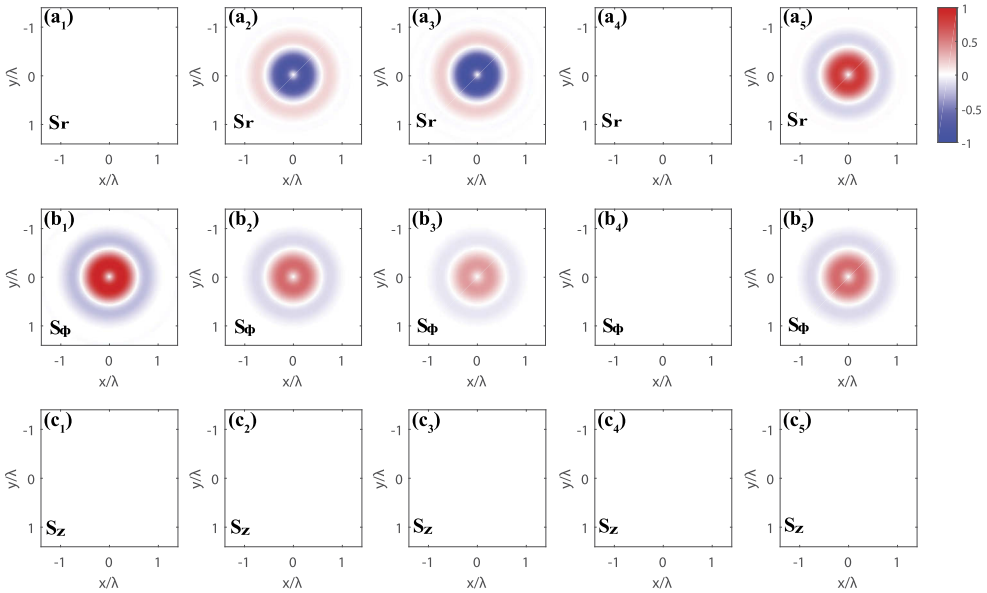

Fig. 3. Normalized SAM density distributions in the focal plane for CVV beams in Fig. 2 with $\varphi_0 = 0, \pi/4, \pi/3, \pi/2$ and $-\pi/4$ from left column to right, respectively. Rows 1-3 are radial, azimuthal and longitudinal components of SAM density.

strongly focused input CVV beams with $\varphi_0 = 0, \pi/6, \pi/4, \pi/3, \pi/2$ and $-\pi/4$ and topological charge $m = 0$ (Figs. 6(a_1)–6(c_1)), $m = 1$ (Figs. 6(a_2)–6(c_2)) and $m = -1$ (Figs. 6(a_3)–6(c_3)). All distributions have been normalized to their maximum values. In Figs. 6(c_2) and 6(c_3), it is demonstrated that the longitudinal SAM densities S_z only exist when there is OAM, i.e., $m \neq 0$. We can see that the sign of S_z changes from positive to negative when the topological charge changes from $m = 1$ to $m = -1$, while the absolute values of the amplitudes remain unchanged. With the increase of initial phase φ_0, the absolute values of S_z increase as well. Conversely, the absolute values of S_ϕ decrease to zero when φ_0 reaches to $\pi/2$ no matter what the topological charge is, seen in Figs. 6(b_1)–6(b_3). Figures 6(a_1)–6(a_3) display that the radial SAM density values are zero when $\varphi_0 = 0$ or $\pi/2$ for any value of m. Moreover, the S_r curves overlap when $\varphi_0 = \pi/3$ and $\pi/6$. From the first column (Figs. 6(a_1)–6(a_3)), one can see that the sign of the initial phase φ_0 only affects the radial spin density. When changing the $\varphi_0 = \pi/4$ to $-\pi/4$, the value of S_r changes from negative to positive. The other two components do not change. As aforementioned discussion in Fig. 3(a_1) and Fig. 5(a_1), with RPV illumination ($\varphi_0 = 0$), the radial SAM density is always zero regardless of the value of m, which agrees well with the results shown in Figs. 6(a_1)–6(a_3). With APV illumination ($\varphi_0 = \pi/2$), one can only produce longitudinal spin density.

Next, we turn to the impacts of the topological charge on the SAM density. Based on the analysis in Fig. 6, the case of $\varphi_0 = \pi/4$ is chosen as a general example. As presented in Fig. 7, S_r and S_ϕ are donut-shaped for all values of topological charge that have been tested. However, for the longitudinal SAM densities S_z, they are donut shapes, only for m>2. In all three components, the density distributions expand from the center to two outer sides and the peak intensity value decreases as the value of m increases. For high m, the peak intensity values are of the same order of magnitude. In fact, the redistributions of SAM densities are caused by the spin flux, which originates from the changes of OAM. As the OAM increases, the dark channel expands from the center of the SAM densities [20]. All of these observations validate the interaction between SAM

Optics EXPRESS

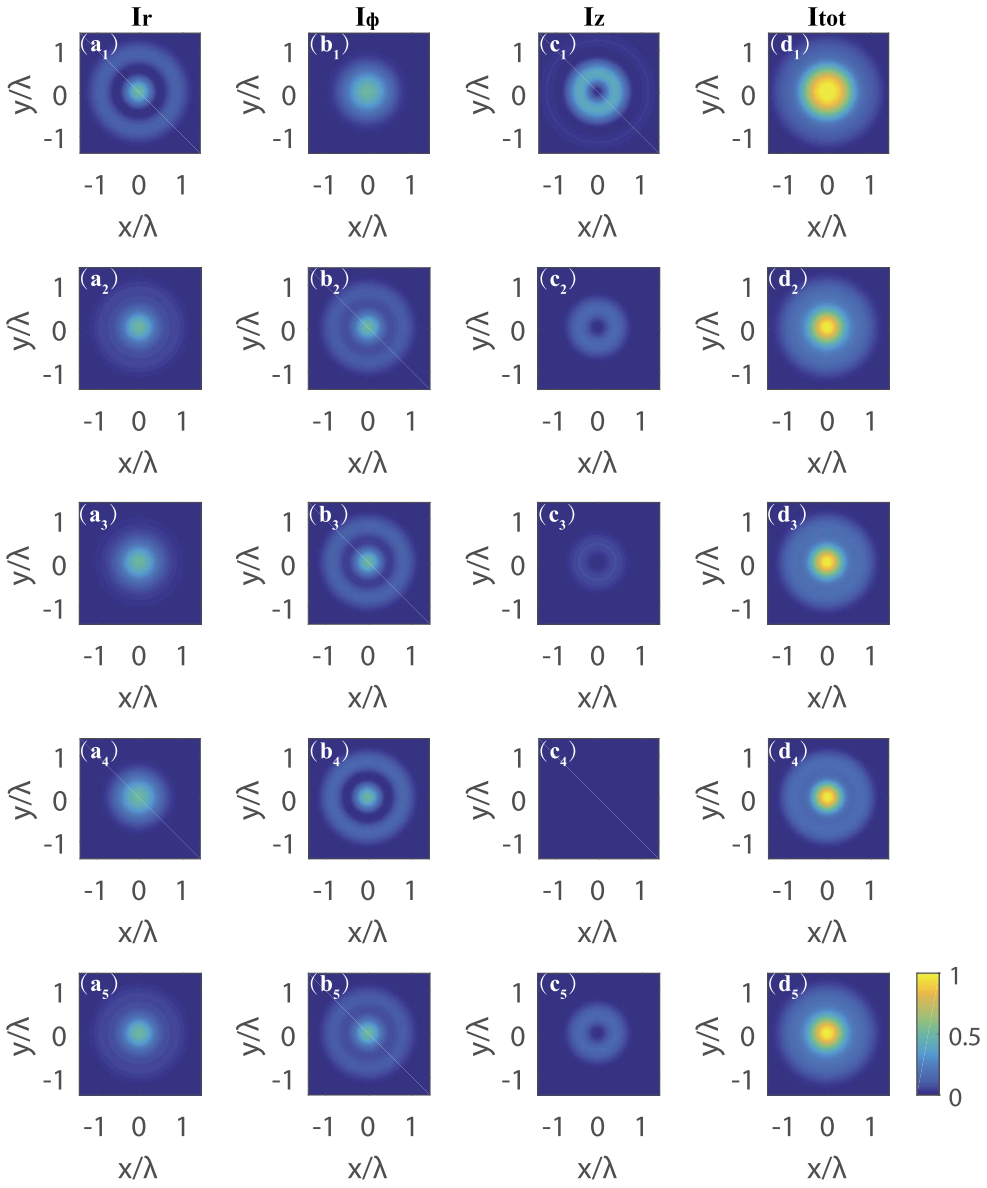

Fig. 4. Electric field intensity distribution in the focal plane of CVV beams with $\varphi_0 = 0$, $\pi/4$, $\pi/3$, $\pi/2$ and $-\pi/4$ (rows 1-5, respectively), when the topological charge $m = 1$. All the intensities are normalized to the maximum intensities near focus for each illumination mode.

Optics EXPRESS

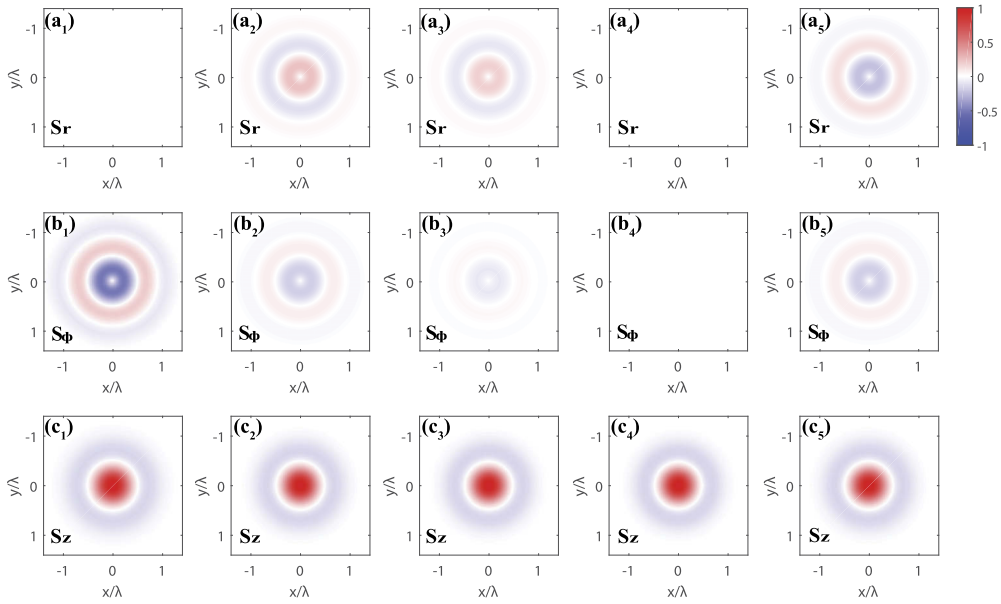

Fig. 5. Normalized SAM density distributions in the focal plane for CVV beams in Fig. 4 with $\varphi_0 = 0, \pi/4, \pi/3, \pi/2$ and $-\pi/4$ from left column to right, respectively. Rows 1-3 are radial, azimuthal and longitudinal components of SAM density.

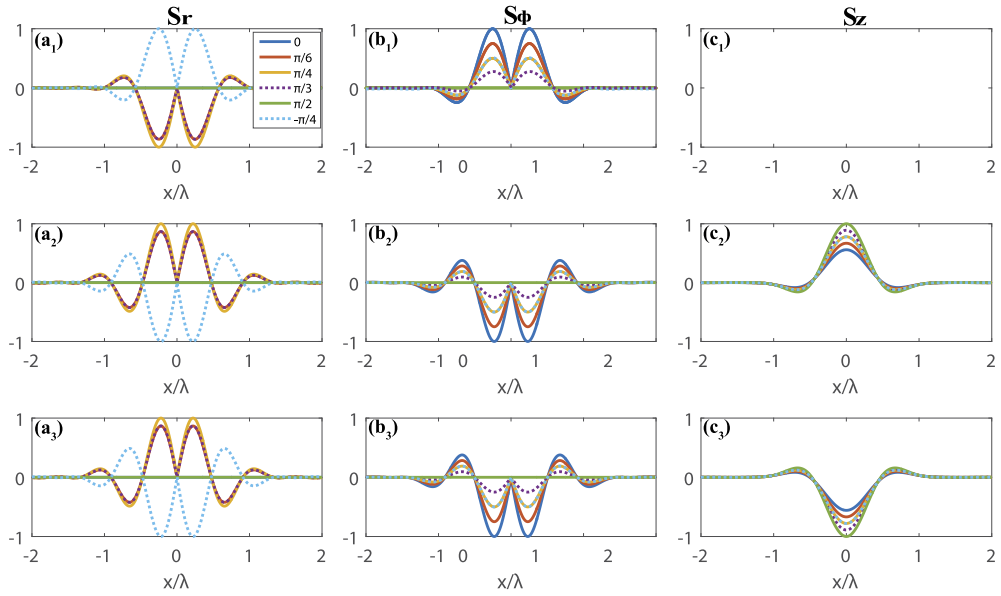

Fig. 6. Normalized cross-sectional electric spin densities in the focal plane of strongly focused input CVV beams with $\varphi_0 = 0, \pi/6, \pi/4, \pi/3, \pi/2$ and $-\pi/4$ and topological charge $m = 0$ (Figs. 6(a_1)–6(c_1)), $m = 1$ (Figs. 6 (a_2)–6(c_2)) and $m = -1$ (Figs. 6 (a_3)–6(c_3)), respectively. The distributions in all plots are normalized to their maximum values.

Optics EXPRESS

and OAM in the tightly focusing process. The above results will be helpful in the application of optical trapping and tweezers.

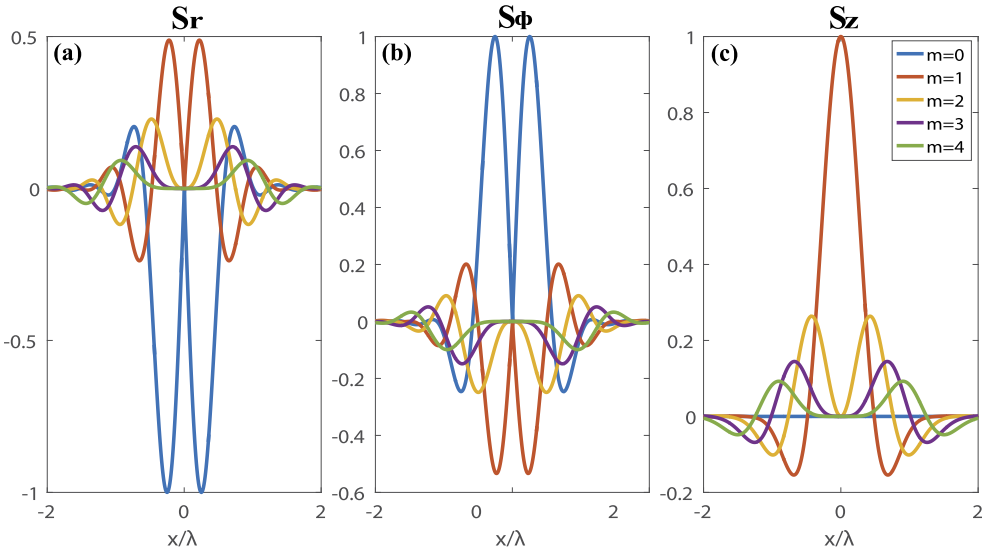

Fig. 7. Normalized cross-sectional electric spin densities (a) radial SAM density S_r, (b) azimuthal SAM density S_ϕ and (c) longitudinal SAM density S_z in the focal plane of strongly focused input CVV beams with $\varphi_0 = \pi/4$ and topological charge changes from 0 to 4. The distributions in all plots are normalized to their maximum values.

3. Optical torque of particles in focused CVV fields

As discussed above, small particles can be trapped due to the localized optical SAM. In other words, the local SAM can also be detected by a small particle. Therefore, we now consider the motion of a Rayleigh sphere with permittivity ϵ_2 in the CVV focal field with a medium of permittivity ϵ_1. The small sphere with a radius a, which should be smaller than the trapping wavelength can be regarded as an electric dipole. The dipole moment is $\mathbf{p} = \alpha\mathbf{E}$ [40–43], where α is the electric polarizability given by

$$\alpha = \frac{\alpha_0}{1 - i(2/3)k^3\alpha_0}, \qquad \alpha_0 = 4\pi\epsilon_1 a^3 \frac{\epsilon_2/\epsilon_1 - 1}{\epsilon_2/\epsilon_1 + 2}, \tag{10}$$

Just like transferring linear momentum from light to a particle generates an optical force on the particle, transferring AM to particle produces an optical torque $\mathbf{\Gamma} = \mathbf{p} \times \mathbf{E}$. When the electric field $\mathbf{E}$ of the CVV beam oscillates harmonically in time, the time-averaged optical spin torque becomes

$$\mathbf{\Gamma} = \frac{1}{2}|\alpha|^2 \mathrm{Re}\left[\frac{1}{\alpha_0{}^*}\mathbf{E} \times \mathbf{E}^*\right], \tag{11}$$

Therefore, the three orthogonal components of the torque are given in cylindrical coordinates by

$$\begin{aligned}
\Gamma_r &= \frac{1}{2}|\alpha|^2 \mathrm{Re}\left[\frac{1}{\alpha_0{}^*}\left(E_\phi E_z^* - E_z E_\phi^*\right)\right], \\
\Gamma_\phi &= \frac{1}{2}|\alpha|^2 \mathrm{Re}\left[\frac{1}{\alpha_0{}^*}\left(E_z E_r^* - E_r E_z^*\right)\right], \\
\Gamma_z &= \frac{1}{2}|\alpha|^2 \mathrm{Re}\left[\frac{1}{\alpha_0{}^*}\left(E_r E_\phi^* - E_\phi E_r^*\right)\right].
\end{aligned} \tag{12}$$

Optics EXPRESS

Figure 8 shows the three-dimensional optical spin torque distributions in the focal plane. An absorptive sphere with refractive index $n_2 = 1.59 + 0.005i$ is placed in a general focused CVV field with topological charges $m = \pm 4$ (Figs. 8(a) and 8(b)) and $\varphi_0 = \pi/4$. The size of the particle is $a = 30nm$. The green arrows indicate the direction of the optical torque, while the magnitude has been normalized. The torque has the same magnitude but opposite direction for opposite signs of m. The reversion is due to the change of the directions of the SAM density shown in Fig. 6. Compared with Eqs. (9) and (12), it is easy to find that the torque is proportional to the SAM density. Figures 8(c) and 8(d) display the motions of the spheres at hot-spots with the corresponding topological charges in Figs. 8(a) and 8(b). The green arrows and circles are the orientations of the spinning and the orbital motions, respectively. The spheres can be trapped at the hot spot of the maximum intensities. Such orientations depend on the illumination polarization as well as topological charge signs.

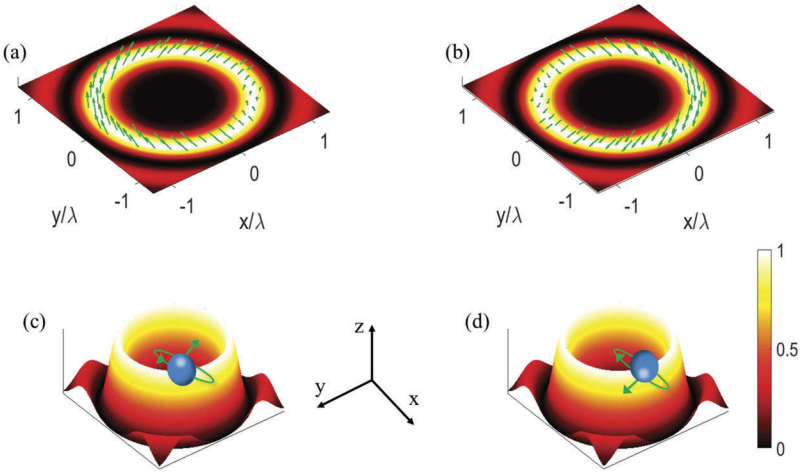

Fig. 8. Three-dimensional optical torque $\mathbf{\Gamma}$ distributions in the focused fields of general CVV beams with $\varphi_0 = \pi/4$ and topological charges (a) m=4 and (b) m=-4. The corresponding spin and orbital motions of trapped absorptive spheres illuminated by the same focal beams with (c) m=4 and (d) m=-4.

Lastly, the influences of the topological charge m (OAM) on the local maximum values of optical torque at the hot-spot position versus the angle φ_0 are presented in Fig. 9. In Figs. 9(a)–9(c), it can be seen that for different topological charges, the three torque components vary as a function of ϕ_0 in similar ways. The maximum longitudinal spin torque at the hot-spot dominates in the three components for any values of angle φ_0. Γ_z starts from minimum value when $\varphi_0 = 0$ and increases gently to the maximum value somewhere when $\varphi_0 = \pi/2$. However, the local maximum azimuthal torque decreases from maximum value to zero till φ_0 increases to $\pi/2$. Meanwhile, the local maximum value of radial torque starts from minimum value zero when $\varphi_0 = 0$, and increases until $\varphi_0 = \pi/4$, then it decreases together with the radial torque till $\varphi_0 = \pi/2$. The amplitudes of the local maximum optical torque decrease with the topological charge increases. In order to make it clear to observe, Figs. 9(d)–9(f) plot variations of each maximal optical torque component at the hot-spot separately. The colors of lines agree with the three components in the above subplots (Figs. 9(a)–9(c)), and different line styles represent different topological charges. The trends in each case are similar to the examples in Figs. 9(a)–9(c). With the increase of m, the values of local maximal optical torques decrease. Another common point is that the fluctuation goes more slightly when m increases, which means the influences of the topological charge on the local maximal values of optical torques at the hot-spot position become tiny, and so as the

Optics EXPRESS

influences come from the initial phase φ_0. Such kinds of examples provide a guide to trapped particle motions and forces with focused CVV beams.

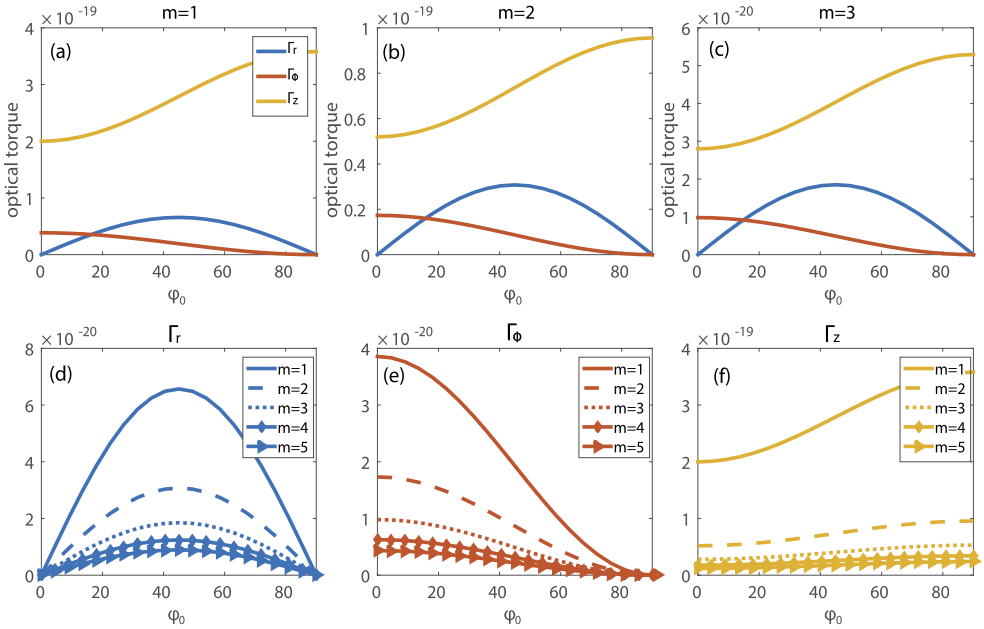

Fig. 9. Three components of local maximum optical torques $\mathbf{\Gamma}$ at the hot-spots in the focused fields of CVV beams with topological charges (a) m=1, (b) m=2 and (c) m=3 versus the angle φ_0 changes from 0 to 2π. Different colors refers to different components: blue-the radial torque, red-the azimuthal torque and yellow-longitudinal torque. For comparison, (d)-(f) show the variations of each maximal optical torque components at the hot-spot as the topological charge changes from 1 to 5 and φ_0 changes from 0 to 2π. Different line styles represent different topological charges.

4. Conclusions

To summarize, we have proposed theoretical investigations on electric field and AM properties of arbitrary highly focused CVV beams. With Richard-Wolf vectorial focusing theory, all components of the electric field near the focus can be obtained, as well as the SAM density produced by the focal field. It is revealed that the properties of the input beam such as the polarization state, the topological charge and initial phase can affect the SAM distribution. The interaction between the SAM and OAM is demonstrated by changing the topological charge m. The redistributions of SAM density are due to the spin flux, which originates from the changes of OAM. The sign of m only changes the direction of longitudinal SAM density and the sign of the initial phase φ_0 only changes the direction of transverse SAM density. An absorptive sphere is placed in the focused CVV field, where it is then trapped. It can be seen that in such tight focal fields, which carry effective SAM, the particle is confined to a hot-spot position of maximal optical torque. As a result, the particle experiences spinning motion. It is found that the orientation of spinning motion depends on the sign of topological charge, the initial phase as well as the polarization of the CVV beam. Thus we can optimize the optical torques by combining different parameters based on the above theoretical simulations. These findings give more freedom for achieving good performance in optical manipulation, trapping and tweezers, beam shaping and directional coupling.

Optics EXPRESS

References

1. L. Allen, S. M. Barnett, and M. J. Padgett, *Optical angular momentum* (Chemical Rubber Company, 2016).
2. D. L. Andrews and M. Babiker, *The angular momentum of light* (Cambridge University, 2012).
3. A. T. O'Neil, I. MacVicar, L. Allen, and M. J. Padgett, "Intrinsic and extrinsic nature of the orbital angular momentum of a light beam," Phys. Rev. Lett. **88**(5), 053601 (2002).
4. L. Allen, M. W. Beijersbergen, R. J. C. Spreeuw, and J. P. Woerdman, "Orbital angular momentum of light and the transformation of laguerre-gaussian laser modes," Phys. Rev. A **45**(11), 8185–8189 (1992).
5. K. Y. Bliokh, E. A. Ostrovskaya, M. A. Alonso, O. G. Rodríguez-Herrera, D. Lara, and C. Dainty, "Spin-to-orbital angular momentum conversion in focusing, scattering, and imaging systems," Opt. Express **19**(27), 26132–26149 (2011).
6. A. Aiello, P. Banzer, M. Neugebauer, and G. Leuchs, "From transverse angular momentum to photonic wheels," Nat. Photonics **9**(12), 789–795 (2015).
7. K. Y. Bliokh, F. J. Rodríguez-Fortu no, F. Nori, and A. V. Zayats, "Spin-orbit interactions of light," Nat. Photonics **9**(12), 796–808 (2015).
8. M. E. J. Friese, T. A. Nieminen, N. R. Heckenberg, and H. Rubinsztein-Dunlop, "Optical alignment and spinning of laser-trapped microscopic particles," Nature **394**(6691), 348–350 (1998).
9. A. Lehmuskero, R. Ogier, T. Gschneidtner, P. Johansson, and M. Käll, "Ultrafast spinning of gold nanoparticles in water using circularly polarized light," Nano Lett. **13**(7), 3129–3134 (2013).
10. J. Ng, Z. Lin, and C. T. Chan, "Theory of optical trapping by an optical vortex beam," Phys. Rev. Lett. **104**(10), 103601 (2010).
11. M. Padgett and R. Bowman, "Tweezers with a twist," Nat. Photonics **5**(6), 343–348 (2011).
12. M. Onoda, S. Murakami, and N. Nagaosa, "Hall effect of light," Phys. Rev. Lett. **93**(8), 083901 (2004).
13. V. S. Liberman and B. Y. Zel'dovich, "Spin-orbit interaction of a photon in an inhomogeneous medium," Phys. Rev. A **46**(8), 5199–5207 (1992).
14. L. Marrucci, C. Manzo, and D. Paparo, "Optical spin-to-orbital angular momentum conversion in inhomogeneous anisotropic media," Phys. Rev. Lett. **96**(16), 163905 (2006).
15. Z. Bomzon, M. Gu, and J. Shamir, "Angular momentum and geometrical phases in tight-focused circularly polarized plane waves," Appl. Phys. Lett. **89**(24), 241104 (2006).
16. A. Canaguier-Durand and C. Genet, "Transverse spinning of a sphere in a plasmonic field," Phys. Rev. A **89**(3), 033841 (2014).
17. K. Y. Kim and S. Kim, "Spinning of a submicron sphere by airy beams," Opt. Lett. **41**(1), 135–138 (2016).
18. M. Li, S. Yan, Y. Liang, P. Zhang, and B. Yao, "Transverse spinning of particles in highly focused vector vortex beams," Phys. Rev. A **95**(5), 053802 (2017).
19. P. Shi, L. Du, and X. Yuan, "Structured spin angular momentum in highly focused cylindrical vector vortex beams for optical manipulation," Opt. Express **26**(18), 23449–23459 (2018).
20. L. Han, S. Liu, P. Li, Y. Zhang, H. Cheng, and J. Zhao, "Catalystlike effect of orbital angular momentum on the conversion of transverse to three-dimensional spin states within tightly focused radially polarized beams," Phys. Rev. A **97**(5), 053802 (2018).
21. M. Li, Y. Cai, S. Yan, Y. Liang, P. Zhang, and B. Yao, "Orbit-induced localized spin angular momentum in strong focusing of optical vectorial vortex beams," Phys. Rev. A **97**(5), 053842 (2018).
22. M. Rashid, O. M. Maragò, and P. H. Jones, "Focusing of high order cylindrical vector beams," J. Opt. A: Pure Appl. Opt. **11**(6), 065204 (2009).
23. J. Pu and Z. Zhang, "Tight focusing of spirally polarized vortex beams," Opt. Laser Technol. **42**(1), 186–191 (2010).
24. S. N. Khonina, "Vortex beams with high-order cylindrical polarization: features of focal distributions," Appl. Phys. B: Lasers Opt. **125**(6), 100 (2019).
25. P. Yu, Q. Zhao, X. Hu, Y. Li, and L. Gong, "Orbit-induced localized spin angular momentum in the tight focusing of linearly polarized vortex beams," Opt. Lett. **43**(22), 5677–5680 (2018).
26. S. N. Khonina and I. Golub, "Generation of an optical ball bearing facilitated by coupling between handedness of polarization of light and helicity of its phase," J. Opt. Soc. Am. B **36**(8), 2087–2091 (2019).
27. T. Omatsu, K. Chujo, K. Miyamoto, M. Okida, K. Nakamura, N. Aoki, and R. Morita, "Metal microneedle fabrication using twisted light with spin," Opt. Express **18**(17), 17967–17973 (2010).
28. A. Ambrosio, L. Marrucci, F. Borbone, A. Roviello, and P. Maddalena, "Light-induced spiral mass transport in azo-polymer films under vortex-beam illumination," Nat. Commun. **3**(1), 989 (2012).
29. S. Syubaev, A. Zhizhchenko, A. Kuchmizhak, A. Porfirev, E. Pustovalov, O. Vitrik, Y. Kulchin, S. Khonina, and S. Kudryashov, "Direct laser printing of chiral plasmonic nanojets by vortex beams," Opt. Express **25**(9), 10214–10223 (2017).
30. G. Milione, T. A. Nguyen, J. Leach, D. A. Nolan, and R. R. Alfano, "Using the nonseparability of vector beams to encode information for optical communication," Opt. Lett. **40**(21), 4887–4890 (2015).
31. S. N. Khonina, A. P. Porfirev, and S. V. Karpeev, "Recognition of polarization and phase states of light based on the interaction of non-uniformly polarized laser beams with singular phase structures," Opt. Express **27**(13), 18484–18492 (2019).
32. Q. Zhan, "Cylindrical vector beams: from mathematical concepts to applications," Adv. Opt. Photonics **1**(1), 1–57 (2009).

Optics EXPRESS

33. V. S. Ignatowsky, "Diffraction by a lens of arbitrary aperture," Trans. Opt. Inst. **1**, 1–36 (1919).
34. E. Wolf, "Electromagnetic diffraction in optical systems-i. an integral representation of the image field," Proc. R. Soc. Lond. A **253**(1274), 349–357 (1959).
35. B. Richards and E. Wolf, "Electromagnetic diffraction in optical systems, ii. structure of the image field in an aplanatic system," Proc. R. Soc. Lond. A **253**(1274), 358–379 (1959).
36. K. S. Youngworth and T. G. Brown, "Focusing of high numerical aperture cylindrical-vector beams," Opt. Express **7**(2), 77–87 (2000).
37. T. Bauer, M. Neugebauer, G. Leuchs, and P. Banzer, "Optical polarization möbius strips and points of purely transverse spin density," Phys. Rev. Lett. **117**(1), 013601 (2016).
38. W. Zhu, V. Shvedov, W. She, and W. Krolikowski, "Transverse spin angular momentum of tightly focused full poincaré beams," Opt. Express **23**(26), 34029–34041 (2015).
39. S. N. Khonina, "Simple phase optical elements for narrowing of a focal spot in high-numerical-aperture conditions," Opt. Eng. **52**(9), 091711 (2013).
40. B. T. Draine, "The discrete-dipole approximation and its application to interstellar graphite grains," Astrophys. J. **333**, 848–872 (1988).
41. P. Meng, S. Pereira, and P. Urbach, "Confocal microscopy with a radially polarized focused beam," Opt. Express **26**(23), 29600–29613 (2018).
42. M. Li, S. Yan, Y. Liang, P. Zhang, and B. Yao, "Spinning of particles in optical double-vortex beams," J. Opt. **20**(2), 025401 (2018).
43. P. C. Chaumet and M. Nieto-Vesperinas, "Time-averaged total force on a dipolar sphere in an electromagnetic field," Opt. Lett. **25**(15), 1065–1067 (2000).